



The role of ferrite in Type 316H austenitic stainless steels on the susceptibility to creep cavitation

A.D. Warren ^{a,*}, I.J. Griffiths ^b, R.L. Harniman ^c, P.E.J. Flewitt ^{a,b}, T.B. Scott ^a

^a Interface Analysis Centre, HH Wills Laboratory, University of Bristol, Bristol BS8 1FD, UK

^b School of Physics, HH Wills Laboratory, University of Bristol, Bristol BS8 1FD, UK

^c School of Chemistry, University of Bristol, Bristol BS8 1TS, UK



ARTICLE INFO

Article history:

Received 24 November 2014

Received in revised form

18 February 2015

Accepted 15 March 2015

Available online 21 March 2015

Keywords:

Type 316 austenitic stainless steel

Magnetic force microscopy

Electron back-scatter diffraction

Creep cavitation

Ferrite

Creep life

R-phase

ABSTRACT

An ex-service Type 316H stainless steel which was subsequently aged at 500 °C for $\sim 22 \times 10^3$ h was found to contain approximately 2% mixed (δ and α) ferrite distributed in localised regions of the microstructure. Preferred creep cavitation at boundaries was associated with these ferrite regions. Creep cavities associated with the austenite–austenite–ferrite boundary junctions, showed a lenticular morphology while austenite–austenite grain boundary creep cavities had a more spherical morphology. Details of the microstructure of these localised regions are described together with the creep cavity distribution. It has been established the extended heat treatment post-service did not result in any significant sintering of creep induced cavities. The results are discussed with respect to the contribution of the ferrite on the nucleation and growth of the creep cavities and the influence on the overall creep behaviour. An evaluation of the impact of low volume fractions of widely dispersed ferrite on the creep life-time of Type 316H stainless steel is discussed.

© 2015 The Authors. Published by Elsevier B.V. This is an open access article under the CC BY license (<http://creativecommons.org/licenses/by/4.0/>).

1. Introduction

Major engineering based industries such as electrical power generation seek to undertake safe, reliable and economic use of components and structures that make up the profile of the plant [1–3]. In the case of the nuclear power generating industry in the UK there is a requirement to extend the operating life of the fleet of Advanced Gas Cooled (AGR) power stations. One particular challenge is associated with the life of stainless steel boiler components that operate within the creep range. For these particular conditions, stainless steels may deform and be life limited by one of several mechanisms depending on the applied stress and temperature [4,5]. An important factor is the potential change in the initial microstructure of the stainless steel over the service life (typically $> 10^5$ h) which can significantly affect the mechanism that controls creep deformation and therefore the creep rate. It has been recognised by many workers for example Bilberger and Gabeling [6], Senior [7] and Chen [8] that creep deformation rate is dependent on the microstructure of the material, temperature, applied stress and state of stress. Moreover

there is a close relationship between creep deformation and creep failure [9,10]. As a consequence the life of service components requires a quantitative understanding of the accommodation of grain boundary creep cavitation damage combined with the influences of changes in the microstructure to provide improved lifetime prediction.

Due to the methods used to manufacture austenitic stainless steels, up to approximately 10 vol% δ -ferrite [11] is frequently retained at room temperature based on the rate of cooling during casting, the composition of the steel or the solidification method [12,13]. In Type 316 and other 300 series steels, δ -ferrite forms during casting of the original ingots, and then transforms to austenite by diffusion of Cr and Ni between the phases; Cr to the ferrite, Ni to the advancing austenite [12–14]. Subsequently the austenite grains nucleate [12–14] and grow into the pre-existing δ -ferrite grains [12,13]. The presence of residual δ -ferrite retained at room temperature has been ascribed to the comparatively slow diffusion of Cr and Ni (compared to the cooling rate) [11,12,15–17], and thus the equilibrium microstructure is not obtained. It is noteworthy that the slow rate of diffusion also leads to inhomogeneities in the distribution of the alloying elements within the stainless steel [8]. The residual δ -ferrite is typically present at interdendritic regions [12], as either stringers (extended bands) or platelets in rolled materials [11,15,16,18], where as they tend to a minimum energy morphology in cast material [12].

* Corresponding author. Tel.: +44 7814430789.

E-mail addresses: Xander.Warren@bristol.ac.uk (A.D. Warren), [I.J.Griffiths@bristol.ac.uk](mailto:I.Griffiths@bristol.ac.uk) (I.J. Griffiths), Rob.Harniman@bristol.ac.uk (R.L. Harniman), Peter.Flewitt@bristol.ac.uk (P.E.J. Flewitt), T.B.Scott@bristol.ac.uk (T.B. Scott).

The evolution of α -ferrite occurs during aging of 300 series austenitic steels, and has been observed at a range of high temperatures and aging times (525 °C/65,000 h [19], 650 °C/60,000 h [20], 700 °C/600 h [21] and 750 °C/25 h [22]). Several studies have demonstrated that this occurs preferentially within Cr and Mo enriched regions which develop as a consequence of $M_{23}C_6$ carbide dissolution [19–22]. Indeed α -ferrite precipitates have been observed adjoining carbide and other precipitates, whilst in other studies carbide dissolution was complete before α -ferrite was observed to nucleate [21]. Thus both local composition and the rate of dissolution of carbide precipitates play a role in the formation kinetics of α -ferrite; these processes can be enhanced by pre-straining and cold working [21]. The morphology of α -ferrite grains varies depending upon where nucleation occurs, for example at austenite grain boundaries compared with grain edges and nodes [21]. Singhal and Martin [22] observed elongated grains of α -ferrite following further aging. Highly faceted α -ferrite precipitates of a triangular-2D morphology, and very low concentration of alloying elements were observed to be closely related to creep cavities [19].

The presence of ferrite precipitates in the austenitic matrix has the potential to change the creep deformation and cavitation behaviour of the material [11,15,16,23]. Any subsequent change in the grain boundary composition as a consequence of either microalloying or impurity element segregation will modify the boundary energy and significantly modify the initiation of creep cavities. Previous studies on creep cavitation in mixed austenite–ferrite steels have focused on material with a banded microstructure, such as duplex steels [15]. Examples are specific casts of Type 304 austenitic steel with pronounced ferrite stringers [11,15,16]. Where the ferrite bands were perpendicular to the direction of the applied stress, a significant decrease in creep life was observed [16]. However in these cases continuously crept specimens showed no cavities, whilst tests including pre-test loading did show cavities at the austenite–ferrite interface [16]. A higher density of cavities was noted at the interphase boundaries compared with austenite grain boundaries. However, a correlation between the presence of creep cavities and carbide precipitates has also been established [8,16].

The difference of in thermal expansion coefficient (ferrite= 13.3×10^{-6} Δcm/K and austenite= 18.3×10^{-6} Δcm/K at 800 K [24,25]) between austenite and ferrite has been observed to introduce residual micro-stresses in duplex steels [26–30]. The micro-strains/stresses were generated at a temperature of 1050 °C [27] followed by cooling to room temperature. In this case the stresses are compressive within the ferrite and tensile within the austenite [26,27,29], and a degree of plastic deformation of the austenite has been observed to accommodate this misfit strain. The distribution of strain between austenite and ferrite when a stress is applied is highly complex [26–32], with meso-scale load sharing between the ferrite and austenite phases [30]. During the initial elastic deformation, ferrite transfers a higher load fraction than austenite due to its greater elastic modulus ($E_\alpha=210$ GPa, $E_\gamma=180$ GPa [33]). However, the actual load per unit area is approximately equal in both phases, due to the higher yield strength of austenite. Since the bcc ferrite has fewer slip systems it is possible for these grains to force the surrounding austenite grains to deform plastically to accommodate the mismatch [30]. This plastic deformation of the austenite grains will modify the compressive internal micro-stresses in the ferrite grain [26,28]. The consensus is that at the micro-scale there is a difference in the partitioning of stresses between the austenite and ferrite phases in situations where the grains do not conform to simple orientation relationships e.g. Kurdjumov–Sachs relationship, where the slip planes in austenite align with those in ferrite, $\{111\}_\gamma/\{110\}_\alpha$ and the directions $\langle 1\bar{1}0 \rangle_\gamma \parallel \langle 1\bar{1}1 \rangle_\alpha$ [26,30]) to allow easy slip

between the grains. The difference in the slip behaviour of austenite and ferrite leads to a pile-up of dislocations on the austenite side of the phase boundary [31]. The dislocations transmitted across the phase boundary to the ferrite grain produce slip [31]. This leads to an inhomogeneous distribution of dislocations within the ferrite precipitate contributing to the increase in the internal micro-stress under load [26,30,32].

This study identifies the effect that a widely dispersed, low volume fraction, of ferrite precipitates within an austenite matrix has on creep cavitation in Type 316H austenitic steels. This includes an investigation into differences in ferrite morphology, interphase and grain boundary misorientation, and size and distribution of ferrite precipitates on the formation of creep cavities.

2. Experimental

The primary material studied was a 25 mm × 10 mm × 10 mm bar of Type 316H austenitic stainless steel, which has been removed from an attachment weldment of a boiler header component which has been subjected to 65,015 h operation in the temperature range 490–530 °C. It was then subjected to further thermal aging for 22,100 h at 550 °C in the laboratory (the specimen is identified as 'ex-service plus 22k h' throughout). The geometry of the sample is shown in Fig. 1, with the location of the specimen analysed in this study shown. The specimen contains both a crack and a section of the weldment/HAZ area together with creep cavities [8,34]. The heat treatment cycle is summarised in Fig. 1b. Creep cavity formation occurs during the loaded step, and a degree of sintering will occur during the unloaded heat treatment step. The composition of the ex-service specimen is given in Table 1.

A series of Type 316H steel specimens of the same cast (and thus composition) as the ex-service specimens were removed from the same reactor after 65,000 h of service, but were subjected to different post-service conditions. These include an additional 500 h creep test; 1000 h at 720 °C; re-solution treating at 1050 °C for 3 h and re-solution treating at 1050 °C for 3 h, followed by subsequent aging of 1000 h at 720 °C. These give an indication of the ferrite content of the material prior to the 22,000 h additional aging. A header specimen taken from a different cast of Type 316H austenitic stainless steel, but representative of material prior to entering service, was also selected. The specimen has similar dimensions to the ex-service component and was cut from the centre of a 63 mm thick header wall section, which was taken from a different cast to the ex-service component. The chemical composition is given in Table 1. The specimen which has been solution treated for 3 h at 1050 °C, followed by a water quench, as part of the manufacturing process. It has not been subjected to any of the post-manufacture service exposure or thermal aging.

Specimens of each steel were consecutively polished with silicon carbide papers and diamond pastes to obtain a 0.25 μm surface finish. Further polishing with 0.1 μm colloidal silica for a period of 24 h was used to obtain a surface which was suitable for electron back-scatter diffraction (EBSD), atomic force microscopy (AFM) and magnetic force microscopy (MFM) evaluation. EBSD analysis was performed in a Zeiss SIGMA FEG-SEM fitted with a high-speed camera (DigiView 3). The EBSD scans were performed by operating the SEM at 30 kV, in high current mode, with the secondary electron imaging mode, with the specimen tilted by 70° to the horizontal. Orientation image mapping (OIM) data collection software (Ametek, Utah, USA), was used to analyse the EBSD data, and all maps shown were subjected to a confidence-index thresholding to remove results with a confidence of less than 10%. The EBSD volume fractions are taken from the mean of

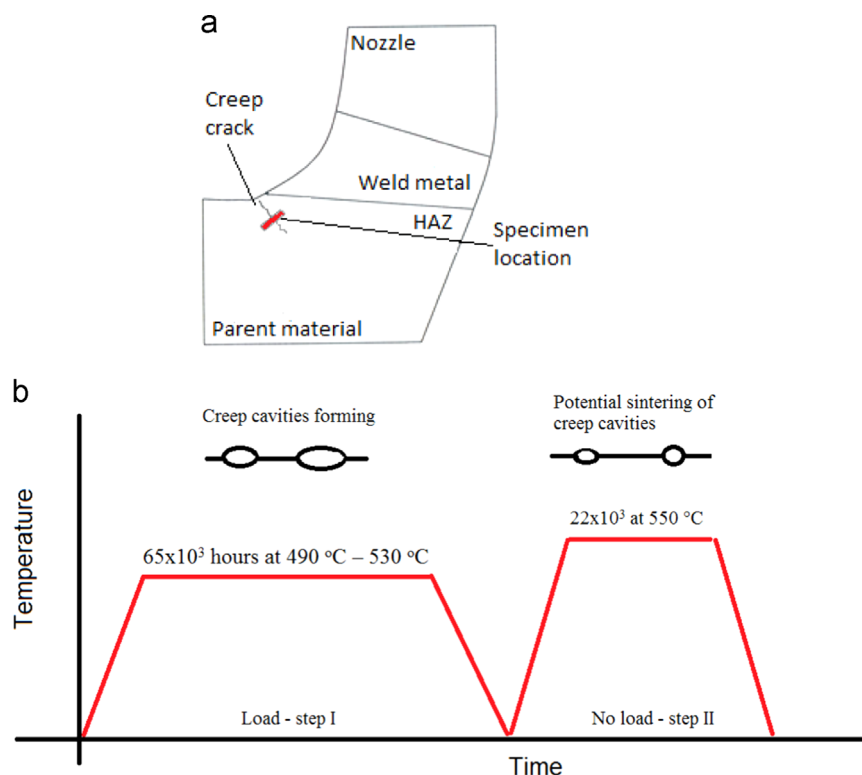


Fig. 1. Schematic diagram showing the ex-service +22k h heat treated component, and a plot of the aging conditions. (a) Diagram of the ex-service component, with the location of the specimen shown in red [8], and (b) diagram showing the aging conditions and the difference in behaviour of creep cavities under these conditions.

Table 1

Composition of the ex-service and pre-service Type 316H austenitic stainless steel header weldment (wt%).

Sample	C	Si	Mn	P	S	Cr	Mo	Ni	B	Co	N	Fe
Ex-service	0.06	0.4	1.98	0.021	0.014	17.17	2.19	11.83	0.005	0.10	—	66.23
Pre-service	0.05	0.52	1.48	0.025	0.01	17.1	2.32	12.0	0.003	0.05	0.033	66.41

3 measurements. Where size of creep cavities is discussed they are characterised as sphere or oblate spheroids and measurement is based on the diameter and the longest axis of the cavities. All EDX and combined EDX/EBSD maps presented were recorded using TEAM V4.1 (EDAX Inc., Mahwah, New Jersey, USA) acquisition software using the same beam settings as for EBSD.

The AFM system used to make the MFM measurements was a Bruker Multimode, fitted with a Nanoscope V controller and a Picoforce extender together with a Budget Sensors Multi75M-G magnetic tip (Innovative Solutions Bulgaria Ltd., Sofia, Bulgaria). The method and optimum settings used for ferrite evaluation is described in another study [34]. Gwyddion 2.30 [35] open source scanning probe microscopy analysis software (<http://gwyddion.net/>; Czech Metrology Institute, Brno, Czech Republic) was used to process the MFM data, with quantification done using a combination of manual and automated thresholding as per the previous study.

A FEI Helios Nanolab 600i ‘Dual beam’ SEM/FIB workstation combined with FEI Slice and View G2 V1.0.1 software (Hillsboro, Oregon, USA) was used to undertake high resolution 3D tomography. Ion beam milling was typically utilised with a resolution of 512 × 442, a beam current of 6.5 nA and a 3 µs dwell; whilst the associated electron beam-secondary electron imaging had a resolution of 1024 × 884, with a beam current of 0.69 nA and a 60 µs dwell time. The slice set was typically 500 slices, each with a width of 100 nm. Reconstruction was done using Amira 5.5.0 (Visage Imaging Inc., San Deigo, California, USA), with cavities identified manually.

Post service samples were characterised by Scanning Transmission Electron Microscopy (STEM) using a JEOL-ARM 200F (JEOL Ltd., Tokyo, Japan), operating at 200 kV. The thin-foils were prepared using the dual-beam FIB allowing accurate placement of the specimen location. A low energy polish of the sample is performed at the end of the etch process to remove surface damage. Chemical analysis has been performed by Energy Dispersive X-ray spectroscopy (EDX) using a 100 mm² Centurion detector and NSS version 3.2 analysis software (Thermo Fisher Scientific Inc., Madison, Wisconsin, USA).

Magneprobe analysis was performed with a Fischer Feritscope FMP30 (Helmut Fischer GmbH, Sindelfingen, Germany) magneprobe. During calibration measurements on a series of standard specimens, the instrument was calculated as having an error of +0.16%. Measurements on the pre-service specimen were made in two locations, both recording 0.0 vol% ferrite, and as such the error is not likely to be significant.

3. Results

In a previous study by Chen et al [36] the ex-service plus 22k h Type 316 austenitic stainless steel specimen was found to contain localised variations in the distribution of Cr and Mo (and impurity elements) arising from the original casting [36]. These localised regions are identified in the optical micrograph, Fig. 2a. The EDX map, Fig. 2b, confirms that these regions contain a higher

percentage of Cr. Creep cavities were observed in the steel, including a proportion of creep cavities which had coalesced to give intergranular cracks such as those in the optical micrograph in Fig. 2a; this confirms the specimen was subject to creep loading during service. Chen's study also indicated that both carbide precipitates and a secondary phase [36] believed to be ferrite were associated with the creep cavities, Fig. 2c.

Large area ($> 5 \text{ mm}^2$) EBSD maps and supplementary local MFM maps (not shown) were prepared and these confirmed that the secondary phase is ferrite. From the EBSD maps it was not possible to determine whether the ferrite was α -ferrite or δ -ferrite. However, the distribution and volume fraction of ferrite could be determined. EBSD gave a volume fraction of approximately 2% α/δ -ferrite following confidence index thresholding, which tallied well with the prediction of 3.04 vol% δ -ferrite given by a Schaeffler–Delong calculation [8]. The α/δ -ferrite typically

took the form of rounded micro precipitates of average size $1.3 \mu\text{m}$ diameter, with a standard deviation of $0.7 \mu\text{m}$. The α/δ -ferrite precipitates were distributed along the austenite–austenite grain boundaries. On some occasions there were linked clusters of several α/δ -ferrite precipitates, Fig. 3.

The pre-service Type 316H stainless steel of a different cast, Table 1, was analysed to determine the probable volume fraction of δ -ferrite in the material. Magneprobe gave a bulk δ -ferrite content of less than 0.1 vol%, which is the maximum sensitivity of the technique. The measurement was repeated with a second magneprobe to confirm the measurement. Large area EBSD phase maps, Fig. 4, revealed the presence of highly dispersed δ -ferrite precipitates with an average size of approximately $5 \mu\text{m}^2$. The area fraction was quantified using EBSD as less than 0.1%, correlating well with the magneprobe data. A Schaeffler–Delong calculation [8] for this cast composition gave a δ -ferrite volume fraction of 3.7%.

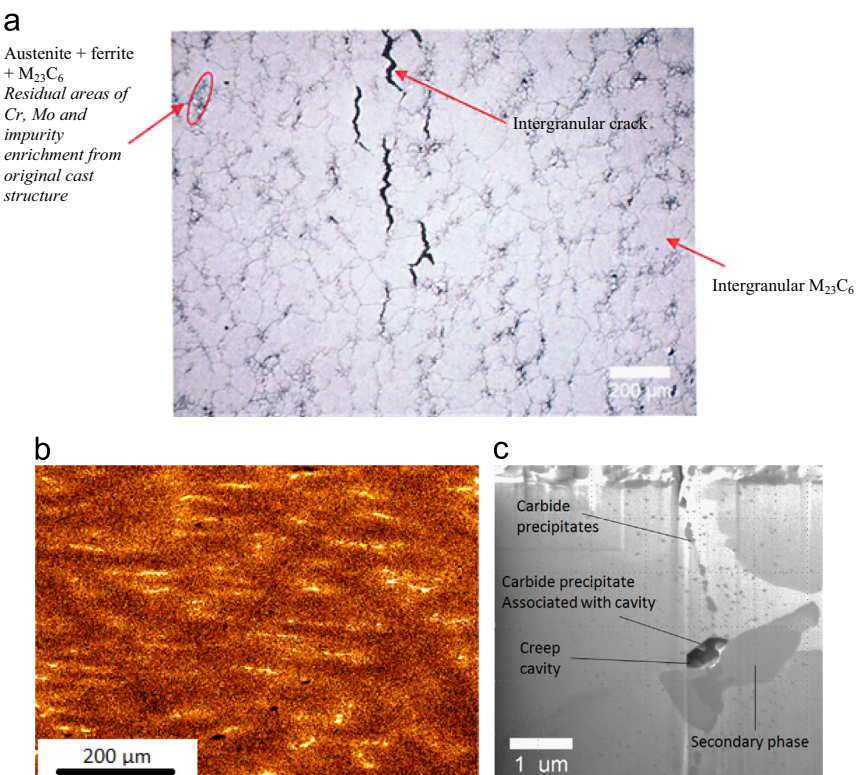


Fig. 2. Characterisation of the ex-service +22k h Type 316H steel specimen. (a) Optical micrograph of the material, showing the localised variation in the material structure [8], (b) Cr specific EDX map, showing the variation in composition. Brighter regions show higher concentrations of Cr. (c) FIB cross-section, showing unknown secondary phase associated with creep cavitation, after Chen et al. [36]. This is representative of sectioned creep cavities from within one of the Cr enriched residual casting regions where secondary phase precipitation predominantly occurs in the specimen.

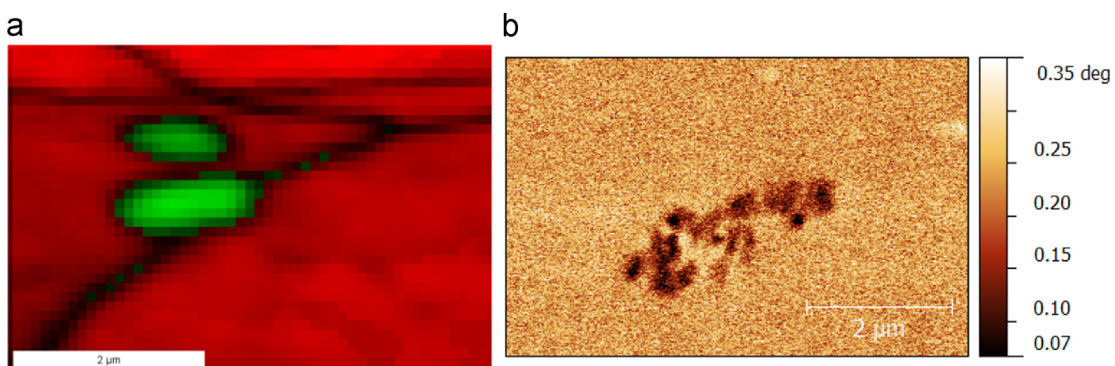


Fig. 3. Microstructural characterisation of the ex-service +22k h Type 316H steel specimen; (a) EBSD and (b) MFM maps from different ferrite precipitates. In the EBSD map, shown in (a) austenite is red and ferrite is green. In the MFM map, shown in (b), the dark regions correspond to the ferromagnetic ferrite. (For interpretation of the references to colour in this figure legend, the reader is referred to the web version of this article.)

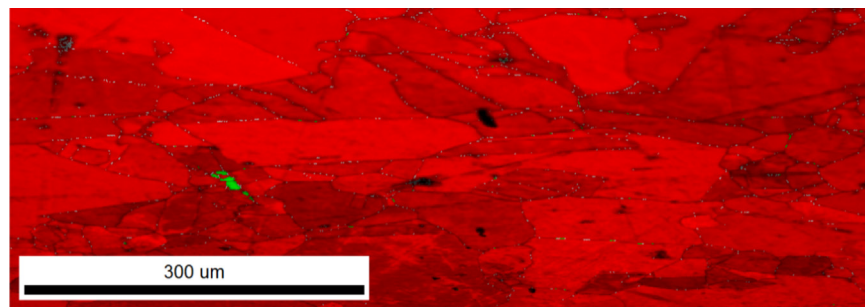


Fig. 4. EBSD map showing the phase distribution in pre-service Type 316H stainless steel. Red grains are austenite, green grains are ferrite and white pixels are points removed during a confidence index threshold. (For interpretation of the references to colour in this figure legend, the reader is referred to the web version of this article.)

Table 2

Aging conditions and magneprobe recorded volume fractions of ferrite measured in the ex-service specimens which had been subjected to less extensive heat treatments.

Condition	Average volume fractions of ferrite (%)
Creep test only (500 h)	0.16
1000 h additional aging at 720 °C	0.16
Re-solution treated at 1050 °C for 3 h	0.19
Re-solution treated at 1050 °C for 3 h, followed by 1000 h additional age at 720 °C	0.15

Several boiler headers from the same cast as the principle specimen were removed from the AGR reactor after 65,000 h (and as such are nominally identical to the principle ex-service plus 22k h specimen). All were subjected to either additional heat-treatments or strain instead of the additional furnace aging. The results of the magneprobe measurements on these specimens are shown in Table 2. Although none of these results are fully representative of the condition of the components upon removal from service after 65,000 h, collectively they show a very low level of ferrite present.

From this it can be concluded that there is either inherent variation in the volume fraction and morphology of δ -ferrite generated during manufacture, or that small volumes of α -ferrite evolve during service. The data is generally randomly scattered consistent with the former. However, observations of low volumes of α -ferrite present after 65,000 h at 525 °C [19], suggests that trace levels of α -ferrite may have evolved towards the end of the materials service lifetime. The majority of the ferrite present during creep will thus be residual δ -ferrite, with an increasing volume of α -ferrite during the later (damage) stages. The additional 22,000 h post service aging experienced by the principle specimen will have led to the formation of α -ferrite post-service, accounting for the additional approximately 1.5 vol% ferrite present in the specimen.

From a previous study [36], the ex-service steel was known to contain creep cavities, Fig. 2c, which were frequently associated with a secondary phase precipitate. In the present study, 780 cavities analysed from across the specimen, 403 (52%) were associated with ferrite – only 9 (0.01%) of which were at ferrite–ferrite grain boundaries. Given the minimal volume fraction of ferrite (less than 0.5%) present in the material prior to the additional 22,000 h heat treatment, the data demonstrates a significant influence of ferrite on the nucleation and/or growth of creep cavities during the overall thermo-mechanical service history of the specimen, Fig. 1b. The EBSD phase map, Fig. 5a (austenite in red, ferrite in green, black features of approximately 1 μm diameter on grain boundaries are creep cavities), and corresponding ferrite specific confidence index map, Fig. 5b (bright tones correspond to higher confidence), show a heavily

creep cavitated austenite grain boundary with a large number of ferrite precipitates. The phase map, Fig. 5a, shows cavities associated with austenite–austenite grain boundaries and austenite–austenite–ferrite boundary “triple point” junctions.

Fig. 6 shows a 3D reconstruction of an MFM map from adjacent to a creep cavity associated with a ferrite precipitate. The structure of the 3D reconstruction corresponds to the topographic data, and as such the dip to the left of the brown feature is the creep cavity. The colouration is taken from the magnetic data – the strength of the colouration corresponds to the degree of interaction between the magnetic probe tip and the specimen, thus the brown regions correspond to ferrite. Faint differences in tone can be observed within the ferrite precipitate, corresponding to magnetic field lines [34]. The units are arbitrary, and depend on several factors including the strength of the magnetic force, the scanning height and the homogeneity of the tip coating.

Combined EBSD-EDX analysis was used to investigate the composition of the ferrite precipitates adjoining creep cavities, to determine if the low alloying element α -ferrite noted in previous work [19] was present in the material. The maps, Fig. 7, showed that approximately 53% of the ferrite grains associated with creep cavitation showed similar levels of Cr and Mo to the bulk austenite (and as such are Cr and Mo depleted compared to the rest of the ferrite precipitates in the mapping region), whilst showing a small enrichment in Fe content. These have been circled in white in Fig. 7. Given the size of many of the precipitates, and the comparative sampling volume of SEM-EDX, contribution from the surrounding grains is almost certainly included in the precipitate data, and as such the higher resolution of STEM-EDX was used to investigate this behaviour further. The TEM foil was cut from a fine grained residual casting region, approximately 100 μm from the edge of the creep crack.

STEM-EDX showed that the low-alloying element α -ferrite was approximately 85% Fe, which correlates well with the previous study [19]. TEM analysis also showed that these low-alloy α -ferrite precipitates are surrounded by a dense cluster of a variety of secondary phase precipitates, including carbides and silicates, which supports the postulation that the α -ferrite may be formed due to ‘super-sensitisation’ during service [19]. The micro-structure is

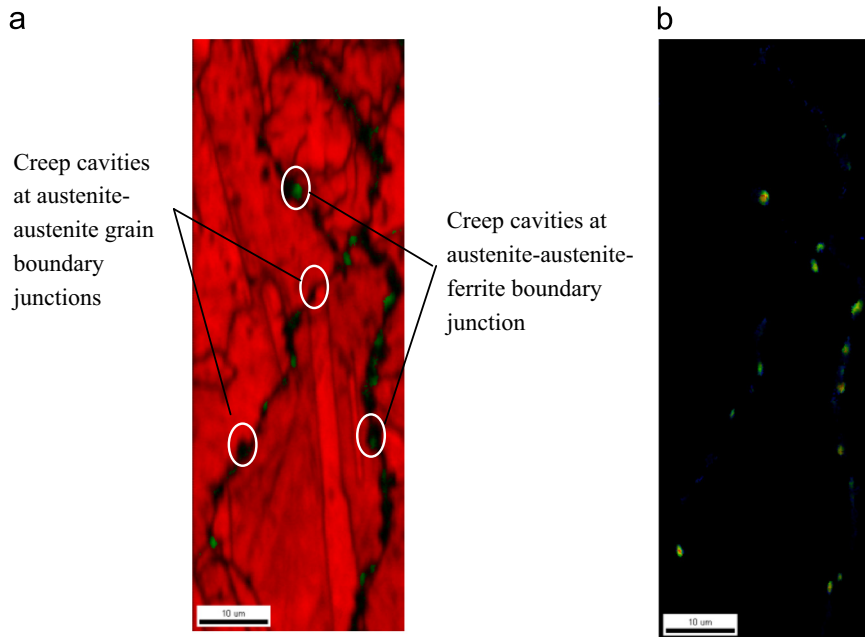


Fig. 5. (a) EBSD map showing the correlation between ferrite and cavities in an ex-service Type 316H steel specimen, where austenite is red, ferrite is green and creep cavities are the black regions. (b) EBSD ferrite specific confidence index map, where the brighter points correspond to the highest confidence. (For interpretation of the references to colour in this figure legend, the reader is referred to the web version of this article.)

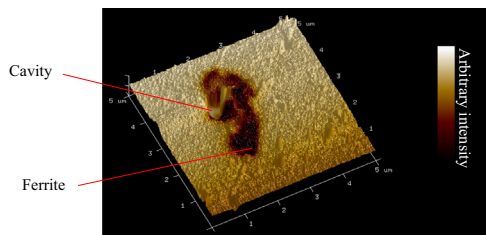


Fig. 6. 3D hybrid image, showing MFM and AFM topography information for the area around a cavity. The AFM topography map has been used to form the reconstruction, with the MFM phase information overlaid. In the MFM data, the darker regions correspond to areas of stronger magnetic signal, with a specimen specific arbitrary scale.

shown in the STEM image in Fig. 8, whilst the corresponding EDX compositions are given in Table 3. The dark semi-circular feature in the top right of Fig. 8 is part of the carbon film used to mount the specimen for analysis, likewise the traces of Ga in the compositions given in Table 3 are the result of the FIB milling required to prepare the specimen.

The compositions of the light precipitates in Fig. 8 are shown in Table 3. Taking the average composition recorded from 13 precipitates of the same contrast in addition to comparable size/morphology, and normalising for the Fe/Ni content gives a composition of $(\text{Fe}, \text{Ni})_{10}\text{Cr}_{5.5}\text{Mo}_{6.3}\text{Si}_{1.3}$, which shows reasonable agreement with the nominal composition of R-phase, $(\text{Fe}, \text{Ni})_{10}\text{Cr}_5\text{Mo}_3\text{Si}_2$ published by Padilha and Rios [37]. There is the possibility that the precipitates are G-phase, and by normalising for Fe/Ni/Mo content gives a composition of $(\text{Fe}, \text{Ni}, \text{Mo})_{16}(\text{Cr}, \text{Mn})_{6.5}\text{Si}_{1.3}$ which shows a weaker correlation with the previously published nominal composition of $(\text{Ni}, \text{Fe}, \text{Mo}, \text{Cr})_{16}(\text{Nb}, \text{Mn}, \text{Cr}, \text{Ti})_6\text{Si}_{60r7}$ [37–40]. Based on the degree of correlation of these compositions the precipitates and are referred to as R-phase in the text. Of the R-phase precipitates 92% were associated with austenite–ferrite boundaries, correlating with the observations of Lai and Haigh [41]. In all cases, the R phase precipitates were associated with ferrite.

In many cases the R phase present in the ex-service plus 22,000 h material showed high levels of Ni, ranging from 8.4 to 32.1 wt%. The R-phase precipitates were typically faceted, and of the order of 50 nm equivalent diameter.

As surface polishing can potentially distort the dimensions of creep cavities [36], 3D tomography was used to investigate the morphology and distribution of cavities in the bulk of the material. The area chosen for analysis was ~1 mm away from the crack edge. Of the creep cavities studied in this region, 85% were found to be lenticular, due to extension along a grain boundary. The majority of these cavities are formed by the agglomeration of two or more smaller cavities. Fig. 9a shows the 3D distribution of cavities (irregularly shaped purple features) in a reconstructed region (bordered by the black lines/green squares), whilst Fig. 9b shows the morphology of several cavities and Fig. 9c shows SEM studies of the specimen surface support cavity ‘agglomeration’.

The net size distribution of cavities as measured by EBSD is given in Fig. 10, and the basic shape of the plot compares well with previous observations for distribution of creep cavity size [42]. Creep cavity size was measured using the diameter of spherical cavities and the longest dimension of elongated/oblate spheroid cavities. Typically the ‘agglomerate’ interlinked cavities tend to be amongst the larger cavities studied, with lengths greater than 6 μm in many cases. The cavities on austenite–ferrite boundaries rather than austenite–austenite–ferrite boundary junctions typically showed extensive interlinkage. The results agree well with a previous, less extensive, study on this material using optical microscopy [36].

Although a fine step-size (<0.5 μm) was used during EBSD mapping, it is possible that submicrometre sized cavities were not fully detected or identified, and as such are under represented in the data set. Such under measurement in the EBSD data is supported by cavity size statistics recorded from the 3D tomography, where of the 204 cavities measured from two nearby (<500 μm) slice and view regions, the average size was 0.7 μm, ranging between 0.2 and 3.1 μm with a similar distribution to the EBSD data. There appeared to be no change in the cavity size distribution through a slice region. The minimum cavity nucleation diameter was calculated as 180 nm [8,43].

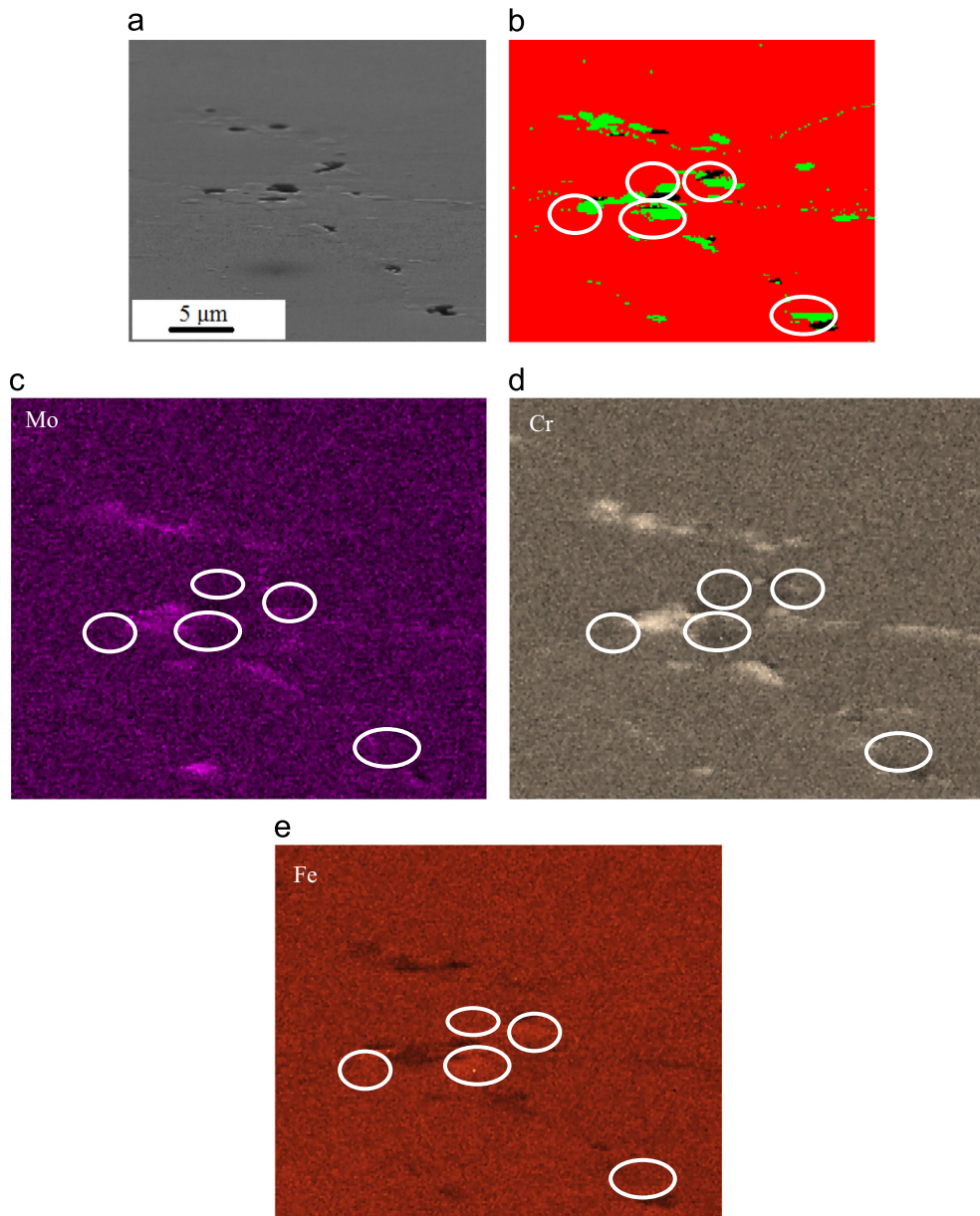


Fig. 7. Elemental EDX maps showing the presence of alloying elements related to the α -ferrite shown in (a) an SEM image of the sample region (including creep cavities) and (b) the corresponding EBSD phase map. The red grains are austenite and the green precipitates are ferrite. (c) is the Mo distribution, (d) the Cr distribution and (e) the Fe distribution. The ferrite regions, circled for clarity, have characteristically low alloying element concentrations and slight Fe enrichments. (For interpretation of the references to colour in this figure legend, the reader is referred to the web version of this article.)

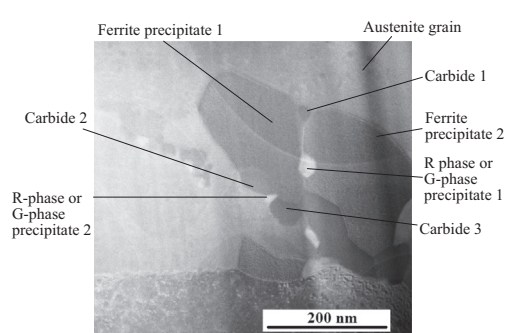


Fig. 8. Annotated STEM image from a Cr rich region, showing two low alloy α -ferrite grains between three austenite grains and the surrounding secondary phase precipitates. Locations correspond to the EDX measured compositions given in Table 3.

4. Discussion

The low volume fraction of δ -ferrite present in the pre-service steel was randomly distributed throughout the material, Fig. 4. When the magneprobe measurements for the ex-service specimens without the additional 22,000 h aging, Table 2, were compared to the pre-service specimen, the implications are that there is either a degree of variation in the volume fraction of δ -ferrite retained during casting or that additional α -ferrite forms during the service period, as observed by Burnett et al. [19]. Thus during in service creep of the steel there will be both the original low volume fraction of δ -ferrite and an evolving volume fraction of α -ferrite. However, the majority of α -ferrite present in the specimen formed during the post-service aging, and thus will not have influenced the creep cavitation. Although some clusters of ferrite precipitates were observed in the ex-service material, these were

Table 3

STEM-EDX measured compositions of low alloying element ferrite grains. The locations for the points are shown in figure 7–3.

Weight %	C	O	Al	Si	S	Cr	Mn	Fe	Co	Ni	Ga	Mo
Ferrite precipitate 1	5.19	1.36	0.11	0.17		6.88		82.82		2.45	0.57	0.46
Ferrite precipitate 2	5.25	0.48	0.11			6.88		84.03		2.35	0.51	0.40
Austenite grain	4.41	1.70	0.06	0.45		13.32	1.16	65.26		12.32	0.50	0.83
R-phase or G-phase precipitate 1	5.61		0.14	9.18		22.74		6.00	0.90	32.11		23.32
R-phase or G-phase precipitate 2	17.48	1.11	0.01	7.30		20.38		6.91	0.69	26.92	0.53	18.67
Carbide 1	7.99		0.14			64.89		18.89		3.96		4.13
Carbide 2	20.29		0.04			56.81		16.51		3.20		3.15
Carbide 3	20.38		0.07			56.86		16.89		2.98		2.81

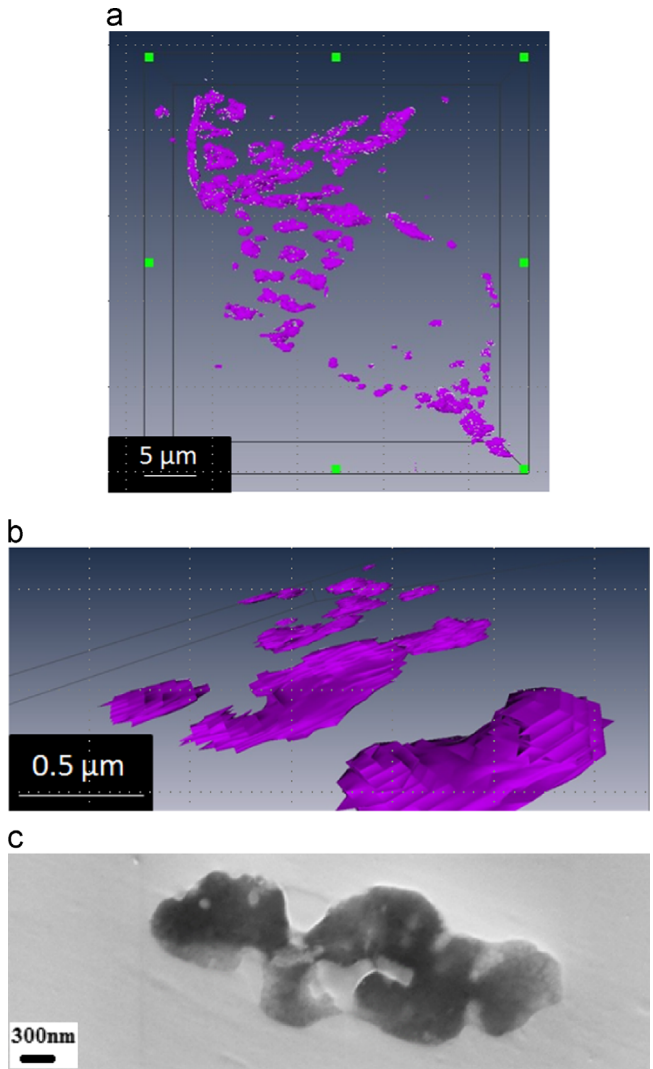


Fig. 9. Sub-surface images of cavities. (a) a 3D ‘slice and view’ reconstruction, with the EBSD imaged sample surface at the top of the reconstruction; (b) the irregular shapes of the larger cavities caused by conglomeration of smaller cavities and (c) the SEM image of a lenticular cavity, which clearly shows signs of being a conglomeration of several smaller cavities.

generally sparse and widely distributed. The region on the right of the image in Fig. 5a is unusual in the number of clusters and comparatively small spacing between the ferrite precipitates.

Previously, creep cavities have been observed to sinter during heat-treatments after the load (stress) has been removed [44,45], and as such it is possible that a degree of sintering may have occurred during the 22,000 h at 550 °C post-service heat treatment.

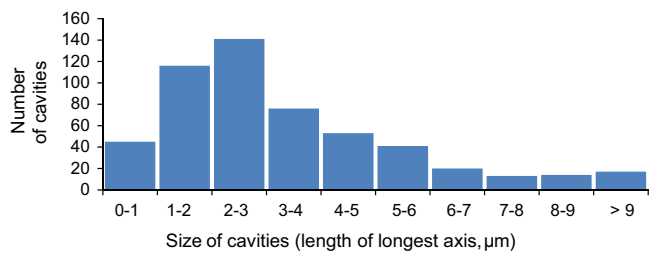


Fig. 10. Net distribution of cavity sizes throughout the sample, as recorded by EBSD. Here the number of cavities within the size categories of 0–1 μm, 1–2 μm, etc. is plotted against each other.

The average rate of sintering, dr/dt , was calculated [44]:

$$\frac{dr}{dt} = \frac{-D_g z \gamma \Omega}{r^3 k T} \left\{ \ln\left(\frac{a}{r}\right) - \left[\frac{(1-(r^2/a^2))(3-(r^2/a^2))}{4} \right] \right\}^{-1} \quad (1)$$

where r is the cavity radius, t is the time and D_g is the grain boundary diffusion coefficient, given by Eq. (2) [45]:

$$D_g = D_0 e^{-Q/RT} \quad (2)$$

z is the grain boundary width, γ is the surface energy, Ω is the atomic spacing, T is the absolute temperature, k is the Boltzmann constant, a is the intercavity spacing, r is the cavity radius, Q is the activation energy and R is the gas constant [44,45]. Data for austenite has been used for the constants [45]: $z=5 \times 10^{-1}$ deg. m, $\gamma=2.2 \text{ J m}^{-2}$, $\Omega=1.18 \times 10^{-29} \text{ m}^3$ and $Q=163.3 \text{ kJ mol}^{-1}$. The 2D EBSD measurements and 3D tomography yield distinctly different values for the inter-cavity spacing, and thus a mean value of $a=1.5 \times 10^{-5} \text{ m}$ has been used and $T=823 \text{ K}$. A plot showing the sintering behaviour of a 3 μm diameter cavity located at an austenite grain boundary over a range of temperatures, Fig. 11, shows there is minimal change in the diameter during aging over a period of 22,000 h ($7.9 \times 10^7 \text{ s}$). The plot demonstrates that at 550 °C the rate of change in cavity size based on the initial cavity dimensions is approximately equal to the rate when the effect of decreasing cavity dimensions is considered.

Using the same equation to determine the sintering behaviour of cavities located on a ferrite grain boundary (γ =the value for austenite [46]), $Q=240 \text{ kJ mol}^{-1}$ [47], $D_0=0.001 \text{ m}^4/\text{Js}$ and $\Omega=2.38 \times 10^{-29} \text{ m}^3$ [48]), no significant sintering occurs during the 22,000 h post-service aging. The sintering equations have been solved numerically using the austenite data and varying initial cavity dimensions to find the cavity size required to yield the mean measured cavity diameter of 1.6 μm after 22,000 h. This gives an initial starting cavity diameter of 2.65 (yielding a constant sintering rate of $6.6 \times 10^{-15} \text{ ms}^{-1}$ by Eq. (1)); which is a close approximation to the rate shown in Fig. 11). This supports the assumptions related to the sintering rates for the 3 μm starting cavity diameter. The morphology and distribution of the ferrite grains in the ex-service +22 h material yields three possible

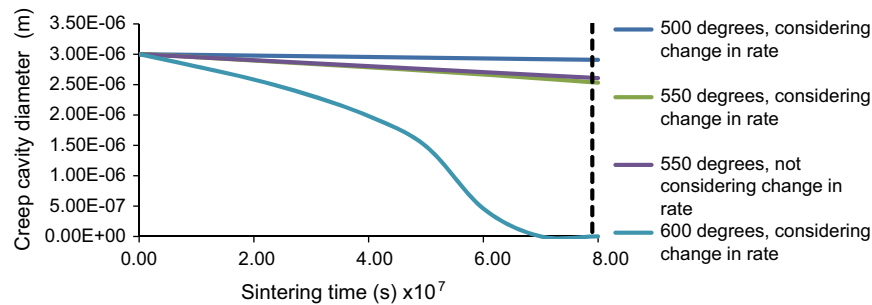


Fig. 11. The change in creep cavity diameter with sintering time for a range of temperatures. The dashed line corresponds to 22,000 h.

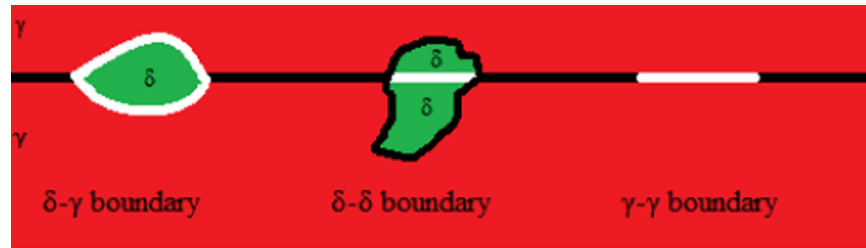


Fig. 12. Schematic showing the three potential locations for cavity nucleation in austenitic steels containing widely dispersed ferrite precipitates. Note that although δ -ferrite is stated, the ferrite grains in the material may be the evolving low-alloy α -ferrite precipitates. The ferrite–ferrite boundary does not have to be aligned with the austenite–austenite boundary.

types of cavity nucleation site, shown schematically in Fig. 12; austenite–ferrite phase boundaries (Fig. 5), austenite–austenite grain boundaries (Fig. 5) and ferrite–ferrite precipitate boundaries (Fig. 8). Due to the random distribution and low volume fraction of ferrite in the steel during creep, the latter case is in the minority (9/780 cavities studied).

Not all ferrite precipitates observed in the 2D scans were visibly associated with creep cavities, Fig. 7. It is assumed the majority of the ferrite precipitates not associated with creep cavities are α -ferrite, which formed during the post-service heat treatment. The majority (80%) of cavities associated with ferrite precipitates were typically sited at the austenite–austenite–ferrite boundary junctions, Fig. 13a. The cavities at these junctions tended to be elongated/lenticular in shape, whilst those that initiated at the austenite–austenite grain boundaries were approximately spherical, Fig. 13b, and shown schematically in Fig. 14a. The faceted nature of the creep cavities prevents these cavities from being truly spherical. Although the circular cavities shown in the 2D EBSD phase map in Fig. 13b have the potential to be cross-sections through rod-like cavities, several approximately spherical cavities have been observed during 3D tomography whilst no rod-like cavities have been observed. Only 26% of the cavities associated with austenite grain boundaries were observed at grain boundary triple junctions.

It is unclear whether the R phase precipitates of ~ 50 nm diameter, Fig. 8, play a role in cavity nucleation. 92% of the observed R-phase precipitates were sited at the austenite–ferrite boundary, and the low number of cavities associated with these boundaries compared to the austenite–austenite–ferrite boundary junctions would imply that the contribution of R phase is minimal. As such the mechanism discussed focuses on the role of interphase boundaries. In a complex state of stress, the nucleation and growth of creep cavities by diffusion will be controlled by the principal stress [49]. This is because the driving force for creep cavitation arises from the normal traction stress across the grain boundaries. Such arguments have been applied at the local level, to interphase boundaries when second phase precipitates are present [50]. The Type 316H austenitic stainless steel selected in

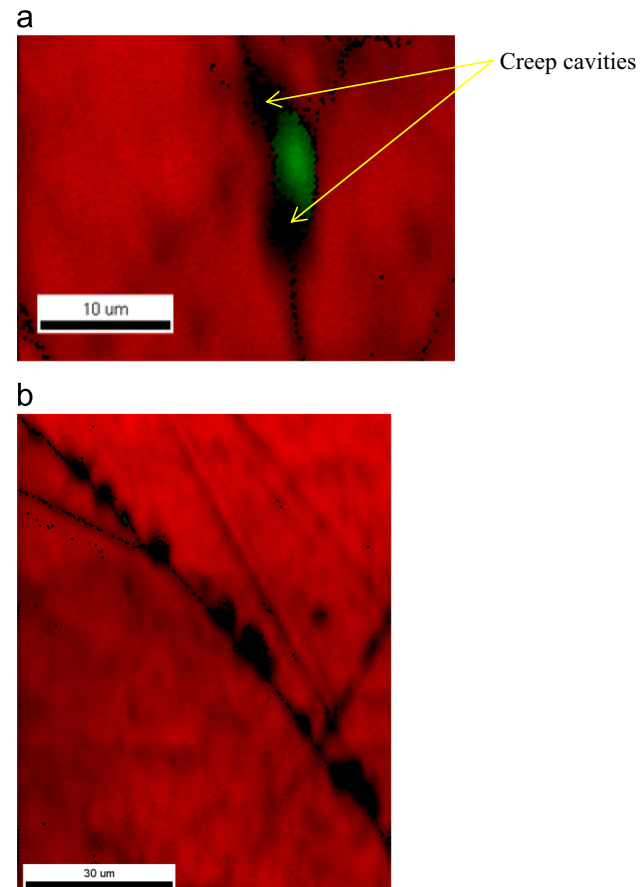


Fig. 13. EBSD phase map showing the typical relationship between cavities, ferrite precipitates and austenite grains. Austenite grains are in red and ferrite precipitates are green. (a) Lenticular creep cavities at the boundary junctions of an abnormally large ferrite precipitate, and (b) spherical cross-section creep cavities on an austenite–austenite grain boundary. (For interpretation of the references to colour in this figure legend, the reader is referred to the web version of this article.)

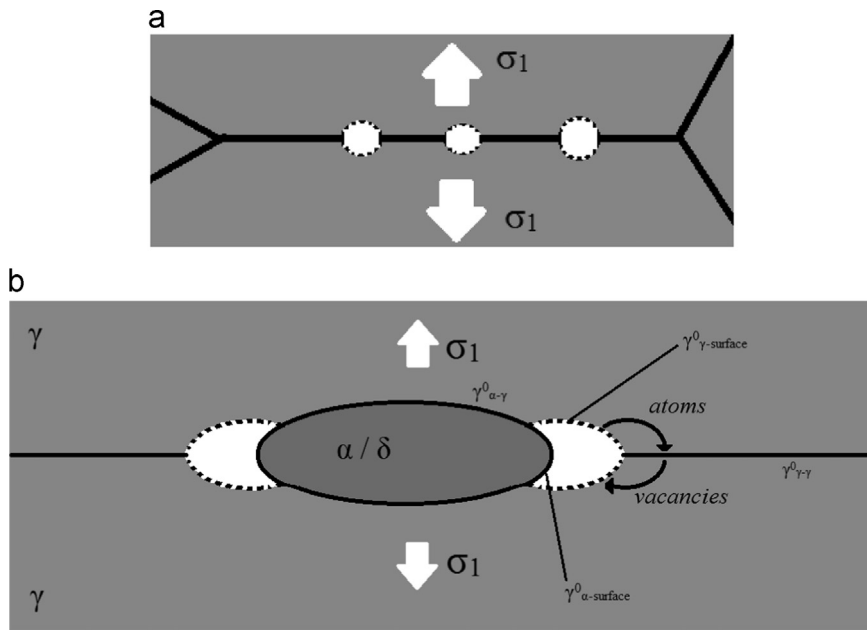


Fig. 14. Schematic diagrams showing the typical morphology of cavities at (a) austenite:austenite grain boundaries and (b) a ferrite precipitate at an austenite grain boundary, the vacancy-atom flow and relative boundary energy values at a The white arrows in the schematics correspond to the direction of maximum principle stress, σ .

this case was subject during service to relatively low stresses such that the component would be operating in a diffusion creep regime. Creep cavity nucleation mechanisms based upon the pile-up of dislocations which lead to subsequent vacancy accumulation have been reviewed by Kassner and Hayes [51]. As considered by Fleck et al. [52] such decohesion at a secondary phase precipitate-matrix grain interface then would extend into the parent grain.

In the present austenitic stainless steel there would be no restriction to such a dislocation pile-up forming. In the Ashby dislocation model [53] as applied by Cane [54] during plastic deformation the build-up of dislocations at a precipitate–matrix interface in a primary glide system can be relaxed by punching dislocation loops in the secondary system. If the movement of these loops is impeded then a back stress will be sustained and developed at the interface. As shown in Fig. 13 the path length would typically be $\leq 5 \mu\text{m}$ in ferrite, so that an appropriate level of back stress can be developed to initiate a creep cavity. Zieliński et al. noted dislocation pile-ups at the austenite– δ ferrite phase boundaries during room temperature plastic deformation of a duplex steel [31] which would support this postulation. The threshold stress, σ_{crit} , required to ensure a stable creep cavity is given by

$$\sigma_{\text{crit}} = \frac{2\gamma^0}{r_{\text{crit}}} \quad (3)$$

where r_{crit} is the cavity radius and γ^0 is the interfacial energy (grain boundary or interphase boundary). This concept of a threshold stress for cavity nucleation arises from a kinetic model where vacancies are considered to cluster to produce stable growing cavities once the critical size is achieved [50]. Chen [8] calculated r_{crit} to be 90 nm for a Type 316H austenitic stainless steel. However, in the present consideration which includes an interphase boundary this size will be modified by (i) the uniaxial stress state experienced by the sample extracted from the service component, (ii) the change to the grain and interphase boundary energies due to any local composition arising from segregation at the exposure temperature ($\sim 550^\circ\text{C}$), and (iii) the inhomogeneous distribution of strain within the material. As a consequence nucleation of creep cavities at second phase ferrite precipitates

located at austenite grain boundaries would be favoured [50], as shown schematically in Fig. 14b. Clearly the nucleation barrier is sensitive to the various interfacial energies; $\gamma^0_{\gamma-\gamma}$ austenite grain boundary, $\gamma^0_{\alpha-\gamma}$ ferrite–austenite interphase boundary and $\gamma^0_{\alpha\text{-surface}}$ and $\gamma^0_{\gamma\text{-surface}}$ the respective free surface energies. This provides a complex balance so that the nucleation barrier would be reduced as $\gamma^0_{\gamma-\gamma}$ and $\gamma^0_{\alpha-\gamma}$ increase and $\gamma^0_{\alpha\text{-surface}}$ and $\gamma^0_{\gamma\text{-surface}}$ decrease. Hence the threshold value of the critical cavity size at nucleation will be significantly modified compared with the simple $\gamma^0_{\gamma-\gamma}$ value described above.

Once a cavity with a critical size is stabilised there are potentially a range of models to describe the subsequent growth by vacancy controlled diffusion based on the seminal work by Hull and Rimmer [55]. In general in the simplest form the growth of a cavity is accommodated by a rigid body displacement of the two adjacent grains and the arrows indicate the direction of vacancy and atom flow, Fig. 14b. In general, the various models that address this growth mechanism introduce various, but realistic, boundary conditions [56]. In all cases, vacancies move to the initiated cavities leading to atoms being inserted into the associated grain boundary and there is an overall preference for growth along, in this case, the austenite–austenite grain boundary.

With regard to the implications that enhanced creep cavitation at ferrite precipitates has on the overall service life will depend on the volume fraction and distribution of ferrite formed in such Type 316H stainless steel components. The material studied had 2 vol% ferrite, distributed widely (distance between ferrite precipitates of the order of 10–50 μm) after both aging steps, Fig. 5. As such even if it is assumed that every detected ferrite precipitate observed was present during service, and if the ferrite was completely replaced with a creep cavity this contributes a 2% reduction in the effective cross-sectional area of the material to increase the stress experienced by the component. The increased stress, by definition, leads to acceleration in creep rate. However as shown in Fig. 15 there will only be a marginal increase in the effective stress and associated increase in creep rate.

Since the cavities associated with ferrite precipitates are comparatively widely spaced, Fig. 1a, there will be little potential to link and form a crack. This would require sufficient general austenite–austenite creep cavitation to occur to provide a 3D

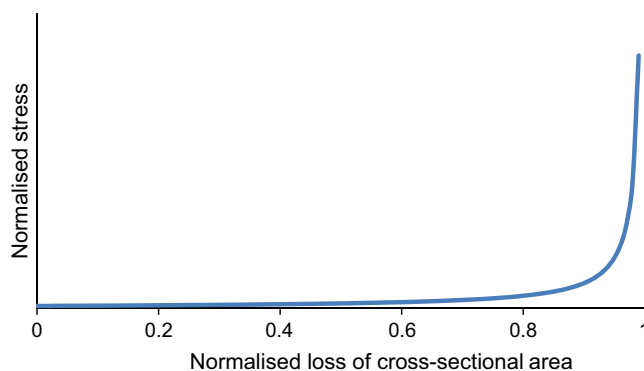


Fig. 15. Plot showing the effect of the loss of cross-sectional area on the stress acting on a component.

linked path within the component to produce overall creep failure. As such the role of such dispersed, low volume fractions of ferrite precipitates on the overall creep behaviour in the present steel will be negligible. It is only of when higher levels of residual δ -ferrite or significant volumes of α -ferrite are formed during service that there is the potential for a more significant effect on service life.

5. Conclusions

The conclusions from this study can be summarised as:

- Chromium rich regions generated during the initial casting process are retained in the fabricated components and these contain a mix of austenite, δ -ferrite and $M_{23}C_6$ carbide precipitates. Although the quantity of residual δ -ferrite will vary inherently, it is believed to be of the order of 0.1 vol% in the steel prior to service.
- During the 65,000 h service exposure at temperatures 490–530 °C, a low volume of α -ferrite evolves, leading to a total ferrite volume of the order of 0.2 vol% following service. During service, creep cavities initiate and grow in the material and there is minimal sintering of creep cavities during the 22,000 h post-service heat treatment at 500 °C. During aging at this temperature approximately 1.8 vol% α -ferrite forms.
- Low volume fractions of very fine R phase or G phase precipitates ~50 nm equivalent diameter were observed to have formed at austenite–ferrite boundaries during service.
- Of the 780 creep cavities studied, >50% were observed to be associated with ferrite grains. The creep cavities were observed to nucleate and grow preferentially at the austenite–austenite–ferrite boundary junctions; and tend to have a lenticular morphology. Cavities at austenite–austenite grain boundaries have a spherical morphology.
- The enhancement of creep cavitation by ferrite precipitates is consistent with the preferential diffusion of vacancies to the austenite–austenite–ferrite boundary junctions.
- Creep cavities associated with the Cr rich regions containing ferrite are widely distributed and would have little influence on the overall creep life of the components made from this steel.

Acknowledgements

Thanks go to EPSRC PROMINENT consortium for the funding for this research; and to EDF Energy for provision of the sample materials, compositions and magneprobe measurements. With thanks to the University of Bristol School of Chemistry Electron Microscopy Unit

(EMU) for use of the MFM equipment and Oxford University Materials department for use of the JEOL ARM 200F. PEJF is grateful to Wolfson College, Oxford for facilitating the collaboration.

References

- [1] P.E.J. Flewitt, in: A. Bakker (Ed.), *Structural Integrity Assessment of High Integrity Structures and Components: User Experience, Mechanical Behaviour of Materials*, Delft University Press, Delft, 1995.
- [2] J.F. Knott *Two Steps From Disaster: The Science of Engineering of Structural Integrity*, Royal Society and Royal Academy of Engineering, London, 1999.
- [3] P.E.J. Flewitt, R. Moskovic, Mater. Sci. Technol. 20 (2004) 533.
- [4] D.G. Morris, Acta Metall. 26 (1978) 1143.
- [5] D.G. Morris, D.R. Harries, Metal Sci. 12 (1978) 525.
- [6] M. Bilberger, J.E. Gibeling, Acta Metall. Mater. 43 (1995) 3247–3260.
- [7] B.A. Senior, Mater. Sci. Eng. A130 (1990) 51.
- [8] B. Chen, *Effects of Thermo-Mechanical History on Creep Damage in 316H Austenitic Steel* PhD thesis, University of Bristol, 2011.
- [9] J. Gittus (Ed.), *Cavities and Cracks in Creep and Fatigue*, Applied Science Publishers, London, 1981.
- [10] C.J. McMahon Jr., Scr. Met. 19 (1985) 733.
- [11] B.S. Rho, H.U. Hong, S.W. Nam, Int. J. Fatigue 22 (2000) 683–690.
- [12] J.W. Elmer, S.M. Allen, T.W. Eagar, Met. Trans. A 20A (1989) 2117–2131.
- [13] G.L. Leone, H.W. Kerr, Weld. Res. Suppl. (1982) 13-s–22-s.
- [14] Th. Schubert, W. Löser, S. Schinnerling, I. Bächer, Mater. Sci. Technol. 11 (1995) 181–185.
- [15] B.S. Rho, H.U. Hong, S.W. Nam, Scr. Mater. 39 (1998) 1407–1412.
- [16] H.U. Hong, B.S. Rho, S.W. Nam, Int. J. Fatigue 24 (2002) 1063–1070.
- [17] H.C. Vacher, C.J. Becholt, J. Res. Natl. Bureau Stand. 53 (1954) 67–76.
- [18] C.C. Tseng, Y. Shen, S.W. Thompson, M.C. Mataya, G. Krauss, Met. Mater. Trans. A 25A (1994) 11471158.
- [19] T.L. Burnett, R. Geurts, H. Jazaeri, S.M. Northover, S.A. McDonald, S.J. Haigh, P.J. Bouchard, P.J. Withers, Mater. Sci. Technol. 31 (2015) 522–534.
- [20] L.P. Stoter, J. Mater. Sci. 16 (1981) 1039–1051.
- [21] W.E. White, I. Le May, Metallography 3 (1970) 51–60.
- [22] L.K. Singhal, J.W. Martin, Acta Met. 16 (1968) 1441–1451.
- [23] C.W. Humphries, N. Ridley, J. Mater. Sci. 9 (1974) 1429–1435.
- [24] F. Cverna, *Thermal Properties of Metals*, 1st Ed., ASM International, Materials Park, Ohio, USA (2002) 9–16, chapter 2.
- [25] Kaye and Layby Online (16th Ed.), National Physics Laboratory, Chapter 2.3.5 Thermal Expansion, Version 1.1 (accessed 21.03. 14), (http://www.kayelaby.npl.co.uk/general_physics/2_6/2_6_6.html).
- [26] J.J. Moverare, M. Oden, Mater. Sci. Eng. A337 (2002) 25–38.
- [27] J. Johansson, M. Oden, X.H. Zheng, Acta Mater. 47 (1999) 2669–2684.
- [28] N. Jia, R. Lin Peng, Y.D. Wang, G.C. Chai, S. Johansson, G. Wang, P.K. Liaw, Acta Mater. 54 (2006) 3907–3916.
- [29] P. Hedstrom, T.-S. Han, U. Liener, J. Almer, M. Oden, Acta Mater. 58 (2010) 734–744.
- [30] J. Johansson, M. Oden, Met. Mater. Trans. A 31A (2000) 1557–1570.
- [31] W. Zieliński, W. Świątnicki, M. Barstch, U. Messerschmidt, Mater. Chem. Phys. 81 (2003) 476–479.
- [32] J.J. Moverare, M. Oden, Metal. Mater. Trans. A 33A (2002) 57–71.
- [33] Engineering Tool Box, Modulus of Elasticity – Young Modulus for some common Materials, (accessed 15.04.14), (http://www.engineeringtoolbox.com/young-modulus-d_417.html).
- [34] A.D. Warren, R.L. Harniman, A.M. Collins, S.A. Davis, C.M. Younes, P.E.J. Flewitt, T.B. Scott, Ultramicroscopy 148 (2015) 1–9.
- [35] D. Nečas, P. Klapetek, Cent. Eur. J. Phys. 10 (1) (2012) 181–188.
- [36] B. Chen, P.E.J. Flewitt, D.J. Smith, C.P. Jones, Ultramicroscopy 111 (2011) 309–313.
- [37] A.F. Padhilha, P.R. Rios, ISIJ Int. 42 (2002) 325–337.
- [38] J.M. Vitek, S.A. David, D.J. Alexander, J.R. Keiser, R.K. Nanstad, Acta Metal. Mater. 39 (1991) 503–516.
- [39] I. Shuroa, H.H. Kuo, T. Sasakib, K. Honob, Y. Todakaa, M. Umemotoa, Mater. Sci. Eng. A 552 (2012) 194–198.
- [40] F.X. Spiegel, D. Bardos, P.A. Beck, Trans. Metal. Soc. AIME 227 (1963) 575–579.
- [41] J.K. Lai, J.R. Haigh, Suppl. Weld. J. (1979) 1–6.
- [42] M.S. Yang, J.R. Weertman, M. Roth, Scr. Met. 18 (1984) 543–548.
- [43] B.F. Dyson, Scr. Metall. Mater. 17 (1983) 31–37.
- [44] R.A. Stevens & P.E.J. Flewitt, The role of hydrostatic pressure on the sintering of creep cavities in a nickel-2% chromium alloy, Acta Met. 1979,27, 67–77.
- [45] R.A. Stevens, P.E.J. Flewitt, Met. Trans. A 14A (1983) 679–686.
- [46] M.K. Veistinen, V.K. Lindroos, Scr. Met. 18 (1984) 185–188.
- [47] L. Chongmo, M. Hillert, Acta Metall. 29 (1981) 1949–1960.
- [48] M. Onink, C.M. Brakman, F.D. Tichelaar, E.J. Mitteijer, S. van der Zwaag, Scr. Met. Mater. 29 (1993) 1011–1016.
- [49] D. Lonsdale, P.E.J. Flewitt, Proc. R. Soc. Lond. A 373 (1981) 491–509.
- [50] R. Raj, Acta. Met. 25 (1978) 995–1006.
- [51] M.E. Kassner, T.A. Hayes, Int. J. Plasticity 19 (2003) 1715–1748.
- [52] R.G. Fleck, D.M.R. Taplin, C.J. Beavers, Acta Metall. 23 (1975) 415–424.
- [53] M.F. Ashby, Philos. Mag. 14 (1966) 1157–1178.
- [54] B.J. Cane, Met. Sci. 10 (1976) 29–34.
- [55] D. Hull, D.E. Rimmer, Philos. Mag. 4 (1959) 673–687.
- [56] A.C.F. Cocks, M.F. Ashby, J. Proc. Mater. Sci. 27 (1982) 189–244.